



**HAL**  
open science

# The 2012 Mw 8.6 Sumatra earthquake: Evidence of westward sequential seismic ruptures associated to the reactivation of a N-S ocean fabric

Claudio Satriano, Eszter Kiraly, Pascal Bernard, Jean-Pierre Vilotte

► **To cite this version:**

Claudio Satriano, Eszter Kiraly, Pascal Bernard, Jean-Pierre Vilotte. The 2012 Mw 8.6 Sumatra earthquake: Evidence of westward sequential seismic ruptures associated to the reactivation of a N-S ocean fabric. *Geophysical Research Letters*, 2012, 39, p. B08409. 10.1029/2012GL052387. insu-03583338

**HAL Id: insu-03583338**

**<https://insu.hal.science/insu-03583338>**

Submitted on 22 Feb 2022

**HAL** is a multi-disciplinary open access archive for the deposit and dissemination of scientific research documents, whether they are published or not. The documents may come from teaching and research institutions in France or abroad, or from public or private research centers.

L'archive ouverte pluridisciplinaire **HAL**, est destinée au dépôt et à la diffusion de documents scientifiques de niveau recherche, publiés ou non, émanant des établissements d'enseignement et de recherche français ou étrangers, des laboratoires publics ou privés.

Copyright

# The 2012 Mw 8.6 Sumatra earthquake: Evidence of westward sequential seismic ruptures associated to the reactivation of a N-S ocean fabric

Claudio Satriano,<sup>1</sup> Eszter Kiraly,<sup>1</sup> Pascal Bernard,<sup>1</sup> and Jean-Pierre Vilotte<sup>1</sup>

Received 19 May 2012; revised 22 June 2012; accepted 29 June 2012; published 3 August 2012.

[1] The 11 April 2012 Mw 8.6 earthquake offshore Sumatra is the largest of the rare great intraplate earthquakes of the instrumental era. This major strike-slip event occurred in the diffuse zone of deformation that accommodates differential rotation between Indian and Australian plates. We perform a back projection analysis – calibrated with well-located aftershocks – of short-period teleseismic P-waves recorded by the European array to image the rupture process during the mainshock. In complement, a Love wave analysis is conducted for tracking azimuthal change in the apparent global source duration due to the source spatio-temporal extent. The combined analysis reveals a complex rupture pattern, characterized by three main episodes of energy release, the latest being located 370 km west of the epicenter, on the Ninety East Ridge, with a delay of 120 s. We interpret the 11 April 2012 Mw 8.6 offshore Sumatra earthquake as a complex westward-propagating sequence of dynamically triggered strike-slip fault ruptures, associated to the reactivation of the inherited NNE–striking sea floor fabric. The dynamic triggering mechanism could result from the interaction between transient surface wave stress perturbations and fluids. **Citation:** Satriano, C., E. Kiraly, P. Bernard, and J.-P. Vilotte (2012), The 2012 Mw 8.6 Sumatra earthquake: Evidence of westward sequential seismic ruptures associated to the reactivation of a N-S ocean fabric, *Geophys. Res. Lett.*, 39, L15302, doi:10.1029/2012GL052387.

## 1. Introduction

[2] On 11 April 2012, a great Mw 8.6 earthquake occurred in the Wharton Basin, 100 km southwest of the Sumatra Trench, and was followed by a major Mw 8.2 aftershock two hours later (Figure 1). These events belong to the diffuse deformation zone of the Indian Ocean that extends between the Chagos-Laccadive Ridge and the Sumatra Trench, accommodating the relative rotation between the Indian and the Australian plates [Wiens *et al.*, 1985]. In this region, the Ninety East Ridge (90ER) acts as mechanical boundary between compressive deformation to the west and strike-slip deformation to the east.

[3] The Wharton Basin (WB) – east of the 90ER – is a wide oceanic left-lateral shear band striking N-S, and is

characterized by an inherited complex fracture zone originating from the extinct Wharton spreading ridge [Deplus *et al.*, 1998]. The diffuse intra-plate seismicity in this region results predominantly from the reactivation of N-S–trending left-lateral strike-slip faults of the fracture zone fabric [Delescluse and Chamot-Rooke, 2007], which can produce large earthquakes, like the 2000 June 18 (Mw 7.9) WB earthquake [Robinson *et al.*, 2001; Abercrombie *et al.*, 2003].

[4] The two 11 April 2012 events are characterized by a predominant strike-slip, left lateral mechanism. The centroid depth range of 18–27 km of the mainshock (<https://geoazur.oca.eu/spip.php?rubrique787>), determined by the SCARDEC method [Vallée *et al.*, 2010], suggests major rupture involving the brittle portion of the mantle, in agreement with some previous seismological [Abercrombie and Ekström, 2001; Robinson, 2011] and experimental [Boettcher *et al.*, 2007; Matysiak and Trepmann, 2012] studies, indicating that brittle deformation can extend into the oceanic mantle down to the 600°C isotherm. Focal mechanisms and locations are in agreement with the active deformation and the inherited sea floor fabric.

[5] A number of rapid kinematic inversions of the April 2012, Mw 8.6 mainshock (see references in the auxiliary material), assuming a single rectangular fault, identify the NNE-SSW nodal plane as the preferred rupture plane, based on aftershock location, optimized fit of waveforms, and orientation of the fracture zone fabric.<sup>1</sup> The occurrence of aftershocks west of the mainshock epicenter, up to the 90ER (Figure 1), raises however the possibility of a NW-SE rupture plane, or of a more complex rupture. To image the rupture process of the April 11 Sumatra mainshock, we combine: a back projection analysis of short-period (0.1–1.0 Hz) P-waves recorded by the European array, after calibration with well-located aftershocks; a study of apparent source duration, at different distances and azimuths, from long-period (20–50 s) Love waves.

## 2. Back Projection Analysis

[6] The back projection (BP) method is a beam forming approach that tracks back the observed coherent short period seismic radiation to the most likely source on the fault plane [e.g., Ishii *et al.*, 2005]. Those short period radiation sources, when imaging extended earthquake ruptures (e.g., M > 8 events at teleseismic distance), are not necessarily co-located with large coseismic slip asperities [e.g., Meng *et al.*, 2011; Satriano *et al.*, 2011; Lay *et al.*, 2012], reflecting

<sup>1</sup>Institut de Physique du Globe de Paris, Sorbonne Paris Cité, Université Paris Diderot, UMR CNRS 7154, Paris, France.

Corresponding author: C. Satriano, Institut de Physique du Globe de Paris, Sorbonne Paris Cité, Université Paris Diderot, UMR CNRS 7154, 1, rue Jussieu, F-75238 Paris CEDEX, France. (satriano@ipgp.fr)

<sup>1</sup>Auxiliary materials are available in the HTML. doi:10.1029/2012GL052387.

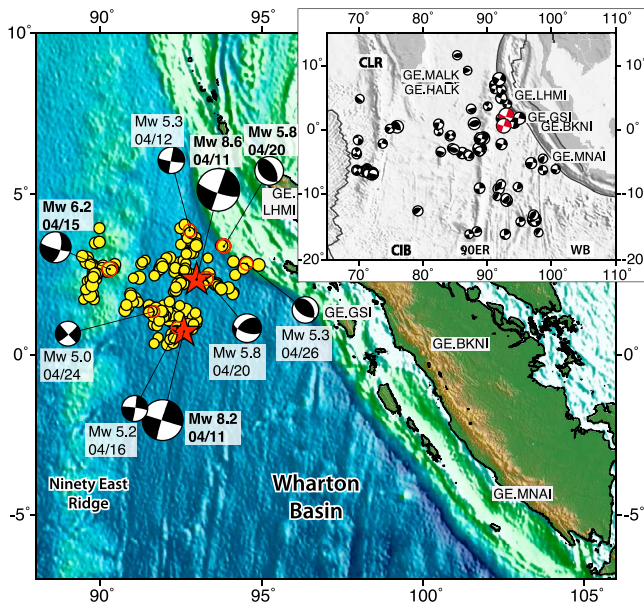


**Figure 1.** The 2012 Sumatra sequence, showing the first 28 days of aftershocks. The two largest events are indicated by red stars; others are represented by yellow circles. Relocated epicenters and revised moment tensor solutions from GEOFON (<http://geofon.gfz-potsdam.de/eqinfo/special/gfz2012hdex>). Bold labels indicate events discussed in the text. Background: composite topography/bathymetry map from Ryan *et al.* [2009] with illumination on the oceanic plate according to free-air gravity anomaly [Sandwell and Smith, 2009]. Inset map: intraplate seismicity up to 2005 compiled by Delescluse and Chamot-Rooke [2007] and location of the two 2012 largest events (in red). CLR: Chagos-Laccadive Ridge; CIB: Central Indian Basin; 90ER: Ninety East Ridge; WB: Wharton Basin. Stations used for the surface wave analysis (Figure 4) are shown on the main map and on the inset. Station AIS (77.57°E, 37.80°S) is not shown.

dynamical complexities due to geometrical or mechanical heterogeneities.

[7] We use a BP method [Satriano *et al.*, 2011] similar to that of Xu *et al.* [2009]. The data set is composed of 204 vertical velocity components of the Virtual European Broadband Seismograph Network (VEBSN, Figure 2a) [van Eck *et al.*, 2004]. The BP analysis is performed in two frequency bands, 0.1–0.5 Hz and 0.5–1.0 Hz. Travel times are computed using a 1D global velocity model [Kennett *et al.*, 1995]. A 4-th root stacking technique [Xu *et al.*, 2009] is used to enhance phase coherency over amplitude coherency, improving resolution at the expense of a possible distortion of relative amplitudes of the energy peaks. Sources of coherent short period radiation are searched on a square grid of 1600 km in size, centered at the mainshock epicenter, with a grid spacing of 20 km (Figures 2b and 2c). At teleseismic distance, the BP method has little or no resolution in depth [e.g., Koper *et al.*, 2012], and the grid is a priori set at depth at 10 km. The BP images are post-processed using a so-called “cube-smoothing” operator, similar to the one proposed by Walker and Shearer [2009], to mitigate sweeping artifacts related to non-destructive interference of incoherent energy.

[8] The horizontal resolution of the BP images can be assessed from the evaluation of the array response function (ARF) [Rost and Thomas, 2002]. The ARF is constructed from BP of monochromatic signals delayed across the network according to the relative travel time from the mainshock epicenter. For each band, we use the lower frequency – namely, 0.1 and 0.5 Hz – to estimate the lowest resolution limit. Figures 2b and 2c show the two resulting ARFs, as normalized maximum power plots. The shape of the ARF is controlled by the effective aperture of the array (in the directions parallel and orthogonal to back azimuth) since waveform coherency breaks down at progressively smaller inter-station distances as frequency is increased [e.g., Xu *et al.*, 2009]. At 1.0 Hz the main coherent contribution is from the central part of the VEBSN, with comparable effective aperture in the two directions, resulting in a nearly circular ARF (Figure 2c). At 0.1 Hz, the ARF is controlled by the whole network geometry, with higher resolution in the direction orthogonal to back azimuth, as a result of the wider aperture of the VEBSN in this direction (Figure 2b).

[9] The departure from 1D velocity model for short period waves – mainly related to lithospheric heterogeneities – cause defocusing of BP images that needs to be corrected.

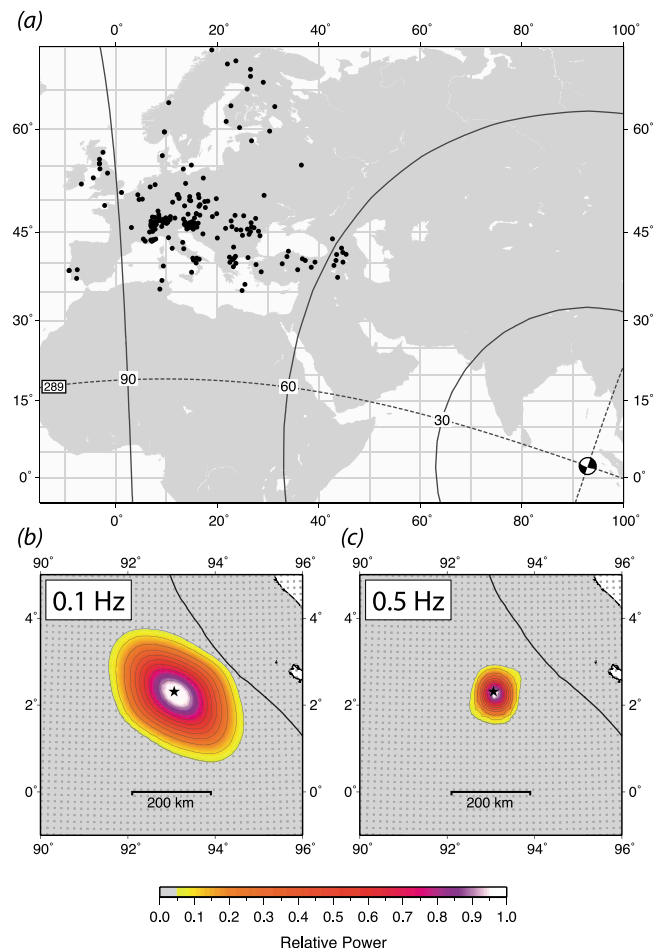


**Figure 2.** (a) Location of the stations (black dots) used for the back projection analysis. (b and c) Array response functions at 0.1 Hz and 0.5 Hz. Back projection grid nodes are indicated by gray dots. Grid spacing is 20 km; grid size is 1600 km × 1600 km (larger than the plot size).

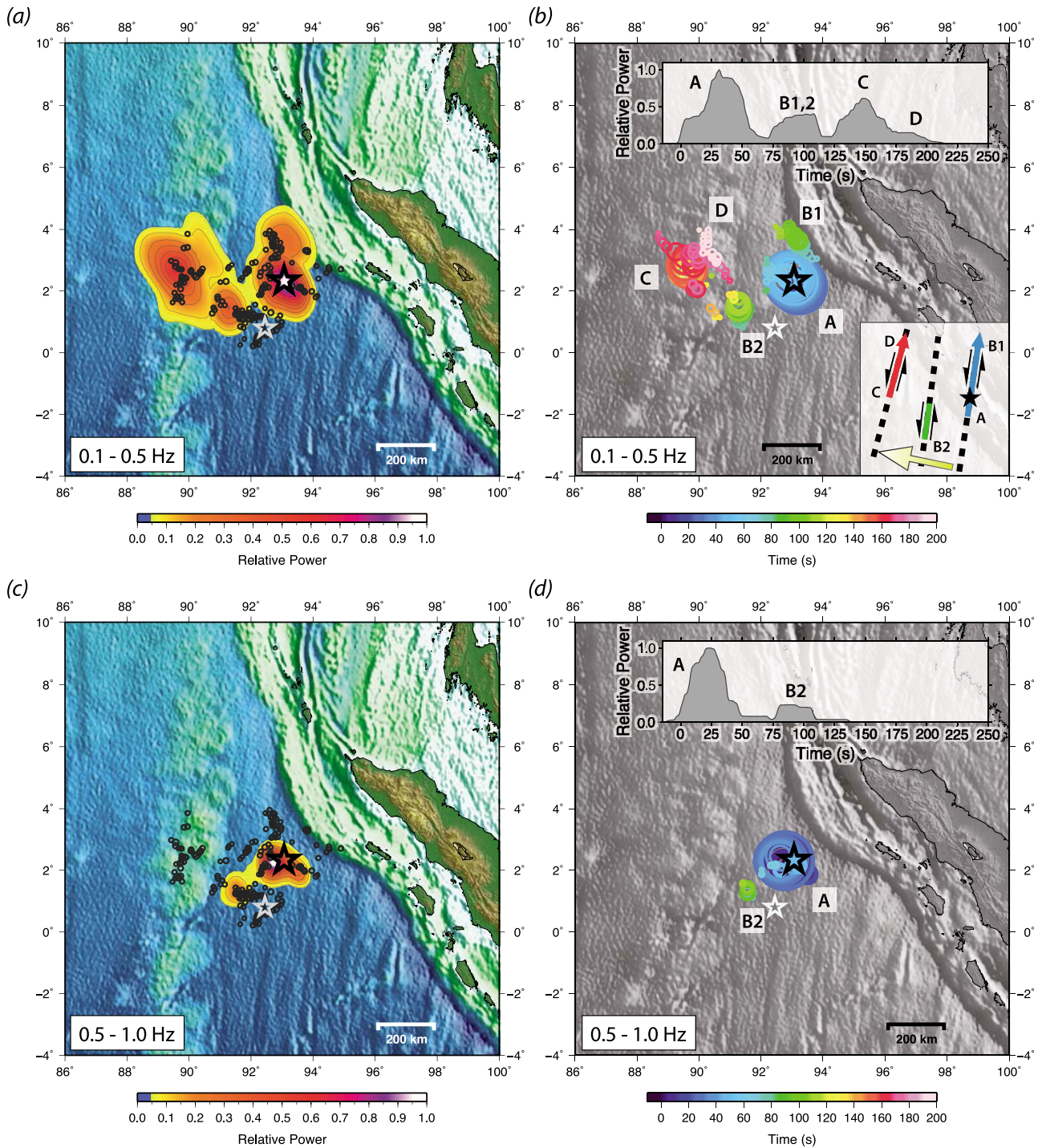


**Figure 3.** Back projection results for the Mw 8.6 mainshock. (a and c) Normalized maximum radiated power in the 0.1–0.5 Hz and 0.5–1.0 Hz frequency bands. Black and white stars are mainshock and largest aftershocks epicenters, respectively; black dots are first 28 days aftershocks. Background as in Figure 1. (b and d) Back projection energy peaks colored by elapsed time and scaled by relative normalized power. Background shading as in Figures 3a and 3c. Top inlets: maximum back projection relative power on the spatial grid as a function of time. Bottom-right inlet in Figure 3b: interpreted rupture mechanism, with yellow arrow indicating westward propagation of the rupture sequence induced by dynamic surface wave triggering.

Residual station corrections are calculated by applying multi-channel cross-correlation [Vandecar and Crosson, 1990] to the first-arrival P waveforms, preliminary aligned according to theoretical travel-times from GEOFON hypocenter (93.14°E, 2.27°N, 10 km depth, origin time:

08:38:35.5 UTC). These station corrections are then used through the whole BP process. The robustness of this calibration step has been verified for two well located aftershocks, as discussed in the auxiliary material.

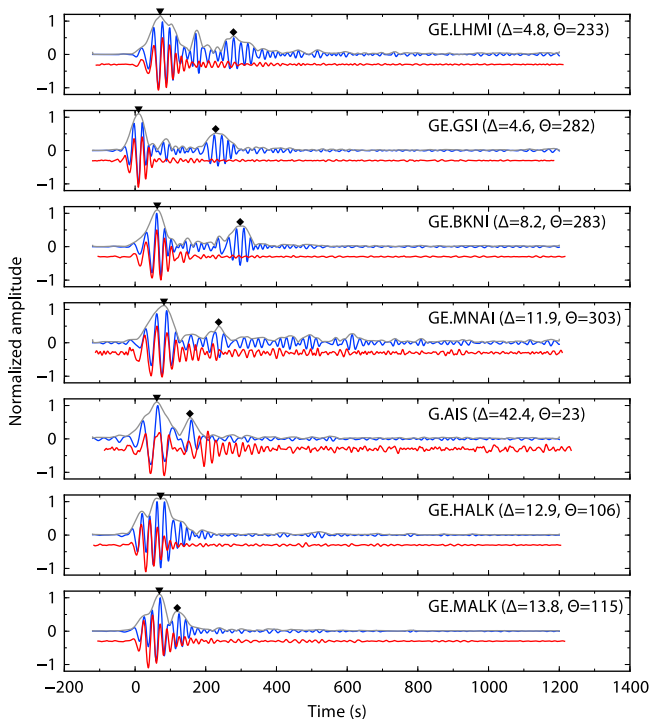


**Figure 4.** Love waves of the mainshock (blue) and of April 20, Mw 5.8 aftershock (red), from the rotated transverse components filtered between 20 and 50 s. For the mainshock, the trace envelope is shown in gray. Station distance ( $\Delta$ , degrees) and back-azimuth ( $\Theta$ , degrees) are indicated after the station name. See Figure 1 for location of events and stations. Triangles and diamonds: observed arrival time of wave packets from subevent A and C, respectively.

[10] Results of the back projection for the mainshock – in the 0.1–0.5 Hz and 0.5–1.0 Hz frequency bands – are summarized in Figure 3. Figures 3a and 3c show the spatial distribution of maximum BP power reached at each grid node during the rupture, as interpolated surface and contour lines. The largest extension of radiative sources is observed for the 0.1–0.5 Hz band, with several radiating episodes between the epicenter area and the 90ER. The maxima of back projected energy are well separated in space, according to the resolution analysis (see Figure 2), and correspond quite well to the aftershock locations (black dots). At higher frequencies (0.5–1.0 Hz), the source appears more compact and mainly concentrated at the epicenter location, with a secondary event to the SW.

[11] Figures 3b and 3d show the spatio-temporal distribution of BP peaks, with amplitude proportional to the relative BP power, and color indicating relative time from the hypocenter. The peaks are extracted using a local maximum filter; therefore multiple local maxima are possible, corresponding to points radiating simultaneously.

[12] The time history in the 0.1–0.5 Hz band shows three main energy events peaking at about 30, 100 and 150 s, and a later, smaller peak at about 190 s. The radiative source remains close to the epicenter location during the first 60–70 s (subevent A on Figure 3b) and then moves northward (subevent B1). At that time, a BP energy radiative source appears to the WSW (subevent B2), about 225 km away from

the epicenter. Finally, a third radiative source (subevent C) appears at 120 s, 370 km west of the main source A; this source is followed by a late burst of energy more to the North (subevent D, starting at 170 s). The apparent SE-NW propagation of the energy peaks within each of the subevents is an artifact due to the distortion of the BP images in the direction of the VEBSN, as evidenced from the ARF at 0.1 Hz (Figure 2).

[13] For the 0.5–1.0 Hz band, the BP is mainly sensitive to the epicenter rupture initiation and to the WSW radiation at  $\sim 100$  s (subevents A and B2). Timing is compatible with that of the 0.1–0.5 Hz band. Resolution in this band is higher and BP images show no significant distortion.

### 3. Surface Wave Analysis

[14] To find evidence of any long period radiation from the third BP source (subevent C), we analyzed its radiated long period (20–50 s) Love waves at different stations, shown in Figure 1. Subevent C being shifted by 370 km to the West from A, an azimuthal variation of the relative timing of the surface waves arrivals is expected, with shorter delay towards West (directive) and longer delay towards East (antidirective). In particular, for antidirective stations, the expected time difference is of the order of  $2 \cdot d/V_g$ , where  $d$  is the distance between the two BP subevents (A and C) and  $V_g$  is the group velocity ( $V_g = 4.4$  km/s). See auxiliary material for additional information.

[15] In Figure 4, transverse component of the Love wave associated to the mainshock is plotted, for different azimuthal directions, together with that of an Mw 5.8 aftershock, used as reference Green's function. Stations located in the eastern quadrant from the source (LHMI, GSI, BKNI) clearly show a distinct, secondary event, delayed by about 200–250 s with respect to the first one. In contrast, stations in the western quadrant (HALK and MALK) show a compact surface wave packet, larger than that of the corresponding Green's function – with difference in duration of about 70 s – close to the duration of the first BP source (subevent A). Finally, the station to the South (AIS) shows a secondary radiation with a delay of about 100 s, which is close to the time delay between the BP sources A and C.

[16] These observations are all compatible with a strong, secondary source of surface waves, coinciding with the third source of the BP (subevent C): the calculated theoretical delays between the Love wave packets from subevents A and C are in agreement with the delays measured from the envelopes in Figure 4, as reported in Table S1 in Text S1. This analysis demonstrates that the third BP source (subevent C) radiates energetic surface waves in the 10–50 s period range and is not an artifact of the back projection. The amplitude of Love waves is about 1 to 1.5 larger than those of the Mw 8.2 aftershock, as evidenced on the records of Eastern stations (PSI, KUM, IPM, BTDF), suggesting a similar moment magnitude for source C.

### 4. Interpretation

[17] The back projection analysis reveals an apparent E-W jerky propagation of the radiative sources during the main shock – with three strong subevents – a complex sequence that cannot be explained by simple rupture propagation along a single N-S strike-slip fault.

[18] One hypothesis is to link subevent C to the earlier sources (A or B2) through westward rupture propagation along a single fault, conjugate to the sea floor fracture zone fabric. A rupture velocity can be estimated as either  $\sim 3$  km/s, from A to C, or  $\sim 3.5$  km/s from B2 to C. This hypothesis is puzzling, since most of the recent large strike-slip intra-plate earthquakes in this region suggest the reactivation of the NNE-trending fracture zone fabric. Even though compound rupture has already been invoked for the 2000 June 18 (Mw 7.9) WB earthquake,  $\sim 2000$  km SSW of the 2012 sequence [Robinson *et al.*, 2001; Abercrombie *et al.*, 2003], the main energy release was associated to the reactivation of a fossil N-S-trending strike-slip fault. Example of a large intra-plate earthquake with compound rupture is the great 25 March 1998, Antarctic plate earthquake [Henry *et al.*, 2000; Antolik *et al.*, 2000; Hjörleifsdóttir *et al.*, 2009] involving two conjugate faults.

[19] In the case of the 2012 offshore Sumatra mainshock, a compound rupture mechanism would involve westward rupture propagation over distances of  $\sim 300$  km, with weak radiation in the period range of tens of seconds (and wavelengths of several tens of kilometers), since no energetic surface waves are detected on the eastern stations before the radiation of source C. Such a smooth rupture propagation with a rather uniform slip velocity distribution at this time and space scales, seems unlikely owing to the many NNE-trending fossil strike-slip faults that would crosscut the rupture path at similar scale (see Figure 3) and generate strength heterogeneities.

[20] Another hypothesis is to associate the strong radiation source C to the dynamic triggering of a N-S-trending strike-slip fault by the most energetic surface waves generated from source A. In this case, a 84 s delay is expected – assuming Love wave group velocity of 4.4 km/s and distance of 370 km between A and C – matching very well the observed 95 s delay between the maximum of surface wave radiation from subevent A (30 s) and the start of subevent C (125 s), in the limit of the ARF resolution and of an almost instantaneous triggering. Furthermore, BP results suggest late northward rupture propagation along the 90ER, from C to D.

[21] We hence propose that this complex earthquake rupture results from a westward propagating sequence of rapidly triggered ruptures possibly reactivating inherited NNE-trending strike faults (subevent C, and possibly B2) at the passage of the surface waves generated from the early phase of the rupture (source A). Subevents B1 and D can possibly be related to northward rupture propagation on reactivated N-S fault structures associated to subevents A and C, respectively. This is also supported by the prevalent SSW-NNE alignment of manually revised aftershock locations, in particular for the latest part of the rupture on the 90E Ridge (Figure 1). This model does not exclude the possibility of some diffuse and smooth E-W rupture components along conjugate strike-slip faults at local scales, that might not be resolved by the back projection analysis.

## 5. Discussions and Conclusions

[22] Since the classical Joshua Tree-Landers-Hector Mine sequence [e.g., Parsons and Dreger, 2000; Kilb, 2003], dynamic stress transfer has been proposed as potential mechanism to enable delayed jumps of the rupture across

distant fault segments, and to trigger remote seismicity at large distances [e.g., Hill *et al.*, 1993; Hough and Kanamori, 2002]. However, evidence of rapid dynamic stress triggering during a single large earthquake event has rarely been reported.

[23] Sequences of dynamically triggered fault ruptures during a single event have been recently observed for the 29 May 2008 (Mw 6.2) earthquake [Hreinsdóttir *et al.*, 2009], in the South Icelandic Seismic Zone, and for the great 25 March 1998 (Mw 8.1) Antarctic earthquake [Henry *et al.*, 2000; Antolik *et al.*, 2000; Hjörleifsdóttir *et al.*, 2009] possibly involving two triggered fault segments at 100 km distance.

[24] At the period of tens of seconds, the triggering potential of Love and Rayleigh waves remains large within the whole depth range of the 2012 Sumatra earthquake. Their combined effects can trigger instantaneous rupture initiation under mixed mode condition [Hill, 2008]. Transient shear stress perturbation, induced by the Love waves, is maximal for strike-parallel and strike-normal incidence on vertical NNE-striking strike-slip faults. Rayleigh wave potential is associated to shear and to interaction between transient dilatational stress perturbation and fluids. For periods of  $\sim 20$  s, coherent pore pressure oscillation cycles – over length scales of  $\sim 80$  km – can lead to transient fault weakening [e.g., Boettcher and Marone, 2004; Hill *et al.*, 1993]. This can be enhanced by the complex fluid pore pressure distributions expected in inherited fracture zone.

[25] Heterogeneous initial stress distribution, suggested by the diffuse seismicity in this region, can control the triggered rupture locations, and the nearly instantaneous rupture initiation. Interestingly enough, no  $M > 5.5$  event is reported in the mainshock area between 1965 and the 2004 Sumatra megathrust earthquake (www.isc.ac.uk), while after 2004, three moderate to large strike slip events (Mw 5.6, 2006/04/19; Mw 6.1, 2007/10/04; Mw 7.2, 2012/01/10) occurred within 50 km of the 2012 epicenter, suggesting possible stress re-arrangements induced by the 2004 earthquake.

[26] The 11 April 2012, Mw 8.6 earthquake provides evidence – as revealed by back projection and Love wave analysis – of a complex rupture sequence reactivating inherited NNE-trending left-lateral strike-slip faults of the oceanic fabric. The rupture is characterized by three main episodes: (1) a major rupture, striking dominantly NNE, and lasting 70 s; (2) a weaker and complex westward propagating sequence of ruptures; (3) a late, powerful source after 120 s, lasting  $\sim 80$  s, and coinciding with the 90E Ridge, 370 km to the West. The latter source C – and possibly source B2 – appears to be dynamically triggered at the passage of the large surface waves from the early rupture. Source C is relatively depleted in high frequencies, suggesting possible slow and coherent slip (see Figure S2 of the auxiliary material).

[27] Great ( $M > 8$ ) intra-plate strike-slip earthquakes are extremely rare. The 2012 Mw 8.6 Sumatra earthquake is the largest ever recorded, the others being the 1998 Mw 8.1 Antarctic plate earthquake and the 2004 Mw 8.1 Tasman Sea earthquake [Robinson, 2011]. A better understanding of dynamic triggering and fault interaction during such events is a necessary step for assessing the seismic potential associated to possible reactivation of similar inherited fracture systems in other oceanic diffuse plate boundary zones.

[28] This study illustrates the importance and the usefulness of teleseismic back projection methods to constrain the space-time evolution of complex large earthquake rupture, avoiding some of the biases associated with a-priori parameterization (fault plane geometry, rupture velocity, and/or slip kinematics). It revealed the late energetic source C, which motivated subsequent surface wave analysis, and provides the main source parameters for future, more complete source analysis, combining body and long period surface waves.

[29] **Acknowledgments.** We thank editor Eric Calais and Martin Mai for their careful review of the manuscript and insightful comments. We also thank Satish Singh and Martin Vallée for discussions at the late stage of this work. This work has been partly supported by the EU Initial Training Network QUEST (QUantitative estimation of Earth's seismic sources and STructure).

[30] The Editor thanks Mai Martin and an anonymous reviewer for assisting in the evaluation of this paper.

## References

- Abercrombie, R. E., and G. Ekström (2001), Earthquake slip on oceanic transform faults, *Nature*, *410*, 74–77, doi:10.1038/35065064.
- Abercrombie, R. E., M. Antolik, and G. Ekström (2003), The June 2000 Mw 7.9 earthquakes south of Sumatra: Deformation in the India–Australia Plate, *J. Geophys. Res.*, *108*(B1), 2018, doi:10.1029/2001JB000674.
- Antolik, M., A. Kaverina, and D. S. Dreger (2000), Compound rupture of the great 1998 Antarctic plate earthquake, *J. Geophys. Res.*, *105*(B10), 23,825–23,838, doi:10.1029/2000JB900246.
- Boettcher, M. S., and C. Marone (2004), Effects of normal stress variation on the strength and stability of creeping faults, *J. Geophys. Res.*, *109*, B03406, doi:10.1029/2003JB002824.
- Boettcher, M. S., G. Hirth, and B. Evans (2007), Olivine friction at the base of oceanic seismogenic zones, *J. Geophys. Res.*, *112*, B01205, doi:10.1029/2006JB004301.
- Delescluse, M., and N. Chamot-Rooke (2007), Instantaneous deformation and kinematics of the India–Australia Plate, *Geophys. J. Int.*, *168*(2), 818–842, doi:10.1111/j.1365-246X.2006.03181.x.
- Deplus, C., M. Diament, H. Hébert, G. Bertrand, S. Dominguez, J. Dubois, J. Malod, P. Patriat, B. Pontoise, and J. J. Sibilla (1998), Direct evidence of active deformation in the eastern Indian oceanic plate, *Geology*, *26*(2), 131–134, doi:10.1130/0091-7613(1998)026<0131:DEOADI>2.3.CO;2.
- Henry, C., S. Das, and J. H. Woodhouse (2000), The great March 25, 1998, Antarctic Plate earthquake: Moment tensor and rupture history, *J. Geophys. Res.*, *105*(B7), 16,097–16,118, doi:10.1029/2000JB900077.
- Hill, D. P. (2008), Dynamic stresses, Coulomb failure, and remote triggering, *Bull. Seismol. Soc. Am.*, *98*(1), 66–92, doi:10.1785/0120070049.
- Hill, D. P. et al. (1993), Seismicity remotely triggered by the Magnitude 7.3 Landers, California, earthquake, *Science*, *260*(5114), 1617–1623, doi:10.1126/science.260.5114.1617.
- Hjörleifsdóttir, V., H. Kanamori, and J. Tromp (2009), Modeling 3-D wave propagation and finite slip for the 1998 Balleny Islands earthquake, *J. Geophys. Res.*, *114*, B03301, doi:10.1029/2008JB005975.
- Hough, S., and H. Kanamori (2002), Source properties of earthquakes near the Salton Sea triggered by the 16 October 1999 m 7.1 Hector Mine, California, earthquake, *Bull. Seismol. Soc. Am.*, *92*(4), 1281–1289, doi:10.1785/0120000910.
- Hreinsdóttir, S., T. Árnadóttir, J. Deciem, H. Geirsson, A. Tryggvason, R. A. Bennett, and P. LaFemina (2009), A complex earthquake sequence captured by the continuous GPS network in SW Iceland, *Geophys. Res. Lett.*, *36*, L12309, doi:10.1029/2009GL038391.
- Ishii, M., P. M. Shearer, H. Houston, and J. E. Vidale (2005), Extent, duration and speed of the 2004 Sumatra–Andaman earthquake imaged by the Hi-Net array, *Nature*, *435*, 933–936, doi:10.1038/nature03675.
- Kennett, B., E. R. Engdahl, and R. Buland (1995), Constraints on seismic velocities in the Earth from traveltimes, *Geophys. J. Int.*, *122*(1), 108–124, doi:10.1111/j.1365-246X.1995.tb03540.x.
- Kilb, D. (2003), A strong correlation between induced peak dynamic Coulomb stress change from the 1992 M7.3 Landers, California, earthquake and the hypocenter of the 1999 M7.1 Hector Mine, California, earthquake, *J. Geophys. Res.*, *108*(B1), 2012, doi:10.1029/2001JB000678.
- Koper, K. D., A. R. Hutko, T. Lay, and O. Sufri (2012), Imaging short-period seismic radiation from the 27 February 2010 Chile (MW 8.8) earthquake by back-projection of P, PP, and PKIKP waves, *J. Geophys. Res.*, *117*, B02308, doi:10.1029/2011JB008576.
- Lay, T., H. Kanamori, C. J. Ammon, K. D. Koper, A. R. Hutko, L. Ye, H. Yue, and T. M. Rushing (2012), Depth-varying rupture properties of subduction zone megathrust faults, *J. Geophys. Res.*, *117*, B04311, doi:10.1029/2011JB009133.
- Matysiak, A. K., and C. A. Treppmann (2012), Crystal–plastic deformation and recrystallization of peridotite controlled by the seismic cycle, *Tectonophysics*, *530–531*, 111–127, doi:10.1016/j.tecto.2011.11.029.
- Meng, L., A. Inbal, and J.-P. Ampuero (2011), A window into the complexity of the dynamic rupture of the 2011 Mw 9 Tohoku–Oki earthquake, *Geophys. Res. Lett.*, *38*, L00G07, doi:10.1029/2011GL048118.
- Parsons, T., and D. S. Dreger (2000), Static-stress impact of the 1992 Landers earthquake sequence on nucleation and slip at the site of the 1999 M = 7.1 Hector Mine earthquake, Southern California, *Geophys. Res. Lett.*, *27*(13), 1949–1952, doi:10.1029/1999GL011272.
- Robinson, D. (2011), A rare great earthquake on an oceanic fossil fracture zone, *Geophys. J. Int.*, *186*(3), 1121–1134, doi:10.1111/j.1365-246X.2011.05092.x.
- Robinson, D., C. Henry, S. Das, and J. Woodhouse (2001), Simultaneous rupture along two conjugate planes of the Wharton Basin earthquake, *Science*, *292*(5519), 1145–1148, doi:10.1126/science.1059395.
- Rost, S., and C. Thomas (2002), Array seismology: Methods and applications, *Rev. Geophys.*, *40*(3), 1008, doi:10.1029/2000RG000100.
- Ryan, W. B. F., et al. (2009), Global Multi-Resolution Topography synthesis, *Geochem. Geophys. Geosyst.*, *10*, Q03014, doi:10.1029/2008GC002332.
- Sandwell, D. T., and W. H. F. Smith (2009), Global marine gravity from retracted Geosat and ERS-1 altimetry: Ridge segmentation versus spreading rate, *J. Geophys. Res.*, *114*, B01411, doi:10.1029/2008JB006008.
- Satriano, C., V. Dionicio, J.-P. Vilotte, and P. Bernard (2011), Using back projection to image earthquake source complexity, Abstract S43C-2253 presented at 2011 Fall Meeting, AGU, San Francisco, Calif., 5–9 Dec.
- Vallée, M., J. Charléty, A. Ferreira, B. Delouis, and J. Vergoz (2010), A new technique for the rapid determination of seismic moment magnitude, focal mechanism and source time functions for large earthquakes using body-wave deconvolution, *Geophys. J. Int.*, *184*(1), 338–358, doi:10.1111/j.1365-246X.2010.04836.x.
- Vandecar, J., and R. S. Crosson (1990), Determination of teleseismic relative phase arrival times using multi-channel cross-correlation and least squares, *Bull. Seismol. Soc. Am.*, *80*(1), 150–169.
- van Eck, T., C. Trabant, B. Dost, W. Hanka, and D. Giardini (2004), Setting up a virtual broadband seismograph network across Europe, *Eos Trans. AGU*, *85*(13), 125, doi:10.1029/2004EO130001.
- Walker, K. T., and P. M. Shearer (2009), Illuminating the near-sonic rupture velocities of the intracontinental Kokoxili  $M_w$  7.8 and Denali fault  $M_w$  7.9 strike-slip earthquakes with global P wave back projection imaging, *J. Geophys. Res.*, *114*, B02304, doi:10.1029/2008JB005738.
- Wiens, D. A., et al. (1985), A diffuse plate boundary model for Indian Ocean tectonics, *Geophys. Res. Lett.*, *12*(7), 429–432, doi:10.1029/GL012i007p00429.
- Xu, Y., K. D. Koper, O. Sufri, L. Zhu, and A. R. Hutko (2009), Rupture imaging of the  $M_w$  7.9 12 May 2008 Wenchuan earthquake from back projection of teleseismic P waves, *Geochem. Geophys. Geosyst.*, *10*, Q04006, doi:10.1029/2008GC002335.